

UNIVERSIDADE ESTADUAL DE CAMPINAS
SISTEMA DE BIBLIOTECAS DA UNICAMP
REPOSITÓRIO DA PRODUÇÃO CIENTÍFICA E INTELECTUAL DA UNICAMP

Versão do arquivo anexado / Version of attached file:

Versão do Editor / Published Version

Mais informações no site da editora / Further information on publisher's website:

<https://link.springer.com/article/10.1140/epjc/s10052-024-13393-2>

DOI: 10.1140/epjc/s10052-024-13393-2

Direitos autorais / Publisher's copyright statement:

©2024 by Springer. All rights reserved.

DIRETORIA DE TRATAMENTO DA INFORMAÇÃO

Cidade Universitária Zeferino Vaz Barão Geraldo

CEP 13083-970 – Campinas SP

Fone: (19) 3521-6493

<http://www.repositorio.unicamp.br>



Measurement of the absolute efficiency of the X-ARAPUCA photon detector for the DUNE Far Detector 1

R. Álvarez-Garrote¹, C. Brizzolari^{2,3}, A. Canto¹, E. Calvo¹, C. M. Cattadori², C. Cuesta¹, A. de la Torre Rojo¹, I. Gil-Botella¹, C. Gotti², D. Guffanti^{2,3}, A. A. Machado⁵, S. Manthey Corchado¹, I. Martín¹, C. Massari^{2,3}, L. Meazza^{2,3,a}, C. Palomares¹, L. Pérez-Molina^{1,b}, E. Segreto⁴, F. Terranova^{2,3}, A. Verdugo de Osa¹, H. Vieira de Souza⁷, D. Warner⁶

¹ CIEMAT, Avda. Complutense 40, 28040 Madrid, Spain

² Dipartimento di Fisica “Giuseppe Occhialini”, Università degli Studi di Milano-Bicocca, Piazza della Scienza 3, 20126 Milan, Italy

³ INFN Sezione di Milano-Bicocca, Piazza della Scienza 3, 20126 Milan, Italy

⁴ Dipartimento di Fisica, Università degli Studi Federico II, 80126 Naples, Italy

⁵ Instituto de Física “Gleb Wataghin”, UNICAMP, Campinas, SP 13083-859, Brazil

⁶ CSU, Limelight Ave, Castle Rock 80109, USA

⁷ Laboratoire Astroparticule et Cosmologie, Rue Alice Domon et Léonie Duquet 10, 75013 Paris, France

Received: 23 May 2024 / Accepted: 20 September 2024 / Published online: 7 October 2024
© The Author(s) 2024

Abstract The DUNE far detector has been designed to detect photons and electrons generated by the charged products of the interaction of neutrinos with a massive liquid argon (LAr) target. The photon detection system (PDS) of the first DUNE far detector (FD1) is composed of 6000 photon detection units, named *X-ARAPUCA*. The detection of the prompt light pulse generated by the particle energy release in LAr will complement and boost the DUNE LAr Time Projection Chamber. It will improve the non-beam events tagging and enable at low energies the trigger and the calorimetry of the supernova neutrinos. The *X-ARAPUCA* is an assembly of several components. Its photon detection efficiency (PDE) depends on the design of the assembly, on the grade of the individual components and on their coupling. The *X-ARAPUCA* PDE is one of the leading parameters for the PDS sensitivity, that in turn determines the sensitivity of the DUNE for the detection of core-collapse supernova within the galaxy and for nucleon decay searches. In this work we present the final assessment of the absolute PDE of the FD1 *X-ARAPUCA* baseline design, measured in two laboratories with independent methods and setups. Preliminary results were reported in Palomares (JINST 18(02):C02064, <https://doi.org/10.1088/1748-0221/18/02/C02064>, 2023). One hundred sixty units of these *X-ARAPUCA* devices have been deployed in the NP04 facility at the CERN Neutrino Platform, the 1:20 scale

FD1 prototype, and will be operated during the year 2024. The assessed value of the PDE is a key parameter both in the NP04 and in the DUNE analysis and reconstruction studies.

1 Introduction

The Deep Underground Neutrino Experiment (DUNE) [2] is a dual-site experiment that aims to measure the neutrino oscillation parameters with a precision and sensitivity that will allow to test the CP violation in the leptonic sector and determine the neutrino mass ordering [3]. It will also perform nucleon decay and beyond standard model searches and it will contribute to the detection of astrophysical neutrinos from the galaxy, the Sun and core-collapse supernova within the galaxy [4]. The DUNE Far detector (FD) will consist of four 17 kt LArTPC modules. This liquid argon (LAr) technology will make possible to reconstruct neutrino interactions with image-like precision. The design of the four identically sized modules is sufficiently flexible for staging construction and evolving the LArTPC technology. The first FD Module (FD1) will use the horizontal drift (HD) technology, in which ionization charges drift horizontally in the LAr under the influence of an electric field towards a vertical anode, where they are read out. Four 3.5 m drift volumes are created between five alternating anode and cathode walls, each wall having dimensions of $(58 \times 12) \text{ m}^2$, and installed inside a cryostat. A schematic of the TPC is shown in Fig. 1.

^a e-mail: luca.meazza@mib.infn.it

^b e-mail: laura.perez@ciemat.es (corresponding author)

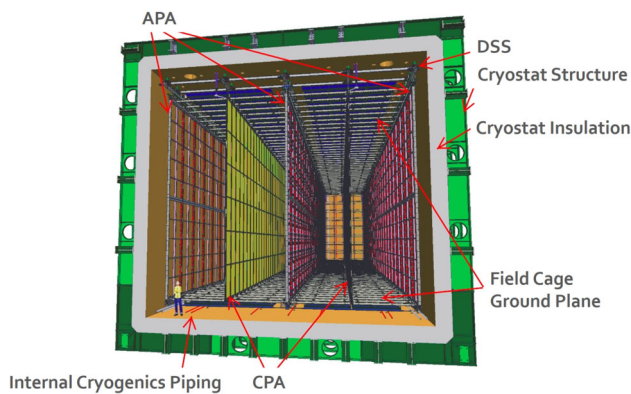


Fig. 1 10 kt DUNE far detector module, showing the alternating 58.2 m long, 12.0 m high anode and cathode planes, as well as the field cage that surrounds the drift regions between the anode (APA) and cathode plane (CPA) [2]

LAr produces abundant VUV scintillation light, emitting 51,000 photons/MeV when excited by minimum ionizing particles in the absence of a drift field [5,6]. The particle's energy losses populate singlet and triplet states of Ar dimers (Ar_2^*), that de-excite with characteristic times of 6 ns and about 1.6 μs respectively, emitting 127 nm photons. The high light yield and its efficient detection will enhance DUNE detector capabilities. To fulfill the supernovae neutrino program and for efficiently tagging nucleon decays, DUNE requires an average light yield of > 20 photoelectrons (PE)/MeV with a minimum > 0.5 PE/MeV, which corresponds to a collection efficiency of 1.3% and 2.6%, respectively [7].

The photon detector system of FD1 consists of light collector modules placed in the inactive space between the inner-most wire planes of the anode planes.

These large-area light collectors convert incident scintillation photons into photons in the visible range that end up in photo-sensors. After investigating many light collector modules, DUNE has successfully reached a design for a light trap that can be deployed as either single-face or dual-face readout, the so-called X-ARAPUCA. In order to validate the DUNE technology, prototypes are being designed, built and tested at CERN, the ProtoDUNEs, LArTPC prototypes of 0.77kt total mass. ProtoDUNE-HD will test the final design of FD1 components at scale 1:1 in 2024. In particular, the X-ARAPUCAs will be tested for the first time there.

2 The X-ARAPUCA device

The X-ARAPUCA (XA) is an improvement of the original concept of photon trapping inside a highly reflective box while using a wavelength shifting (WLS) bar to increase the probability of collecting trapped photons onto a SiPM

array. The ARAPUCA technology has been validated in the run-1 of the ProtoDUNE detector, that showed its superior performances in the photon detection efficiency compared to dip-coated shift lightguides (single or double) [8]. In the XA the entrance window is a glass coated on the external side with a layer of p-Terphenyl (pTP) ($\sim 500\mu\text{g}/\text{cm}^2$) to convert the incident 127 nm scintillation light into isotropically re-emitted 350 nm photons with an efficiency larger than 95%. The re-emitted light reaches the WLS bar where it is further downshifted to the visible range (430 nm), as illustrated in the schematic of Fig. 2a. The WLS re-emitted light can be trapped by total internal reflection ($\theta > 56^\circ$) or escape the WLS bar ($\theta < 56^\circ$) and be reflected by a dichroic filter and by a reflective surface. The filter is a multilayer thin-film coating deposited onto the inner side of the entrance window, whose cutoff is at 400 nm (Fig. 2b). These trapped photons propagate towards the edges of the module where the silicon photo-multiplier (SiPM) photo-sensors are placed. Simulations of the X-ARAPUCA device [9] showed the effectiveness of photon trapping inside the light guide and its dependence on factors such as light guide bulk transmittance, surface reflectiveness and optical coupling with the SiPMs. In DUNE, two different variants will be deployed: a double sided optical window variant, to equip the middle anode plane which collects scintillation photons from both the central drift volumes and a single sided variant to equip the two external anode planes. In this paper the single sided variant has been tested, in which the side opposite to the optical window is an opaque backplane lined inside with an extended specular reflector (ESR). Two different models for the WLS have been tested, the EJ-286 manufactured by Eljen Technology [10] and the other custom designed and manufactured by glass to power (G2P) [11] in collaboration with INFN [12]. Figure 2b shows the emission spectra of both the G2P WLS and the primary wave length shifter. Earlier studies conducted at INFN showed the improved PDE performances of a smaller (or half-size) X-ARAPUCA device, embedding the G2P WLS than with the EJ286 [13]. The SiPM arrays are facing two of the sides of the WLS bar perpendicular to the entrance window. An image taken during the mounting process of an XA installed in Neutrino Platform 04 (NP04) is shown in Fig. 2c. The SiPMs are evenly spaced and an ESR is placed between them on the left empty space on the mounting boards, so that photons reaching the edge of the module not hitting a SiPM are reflected back into the optical module. The SiPM active area is 6x6 mm while the light guide is 4 mm thick so that 1/3 of the area is exposed to the LAr allowing the detection of photons trapped by the dichroic filters.

The module dimensions are 2 m long and 12 cm wide and it consists of 4 XA as shown in Fig. 3a, also known as *Super-cells*. In Fig. 3b we can see that each XA is composed of 6 dichroic filters, 1 WLS bar and 48 SiPMs grouped in 8 PCB boards (6 SiPMs each); the bias and signals are routed

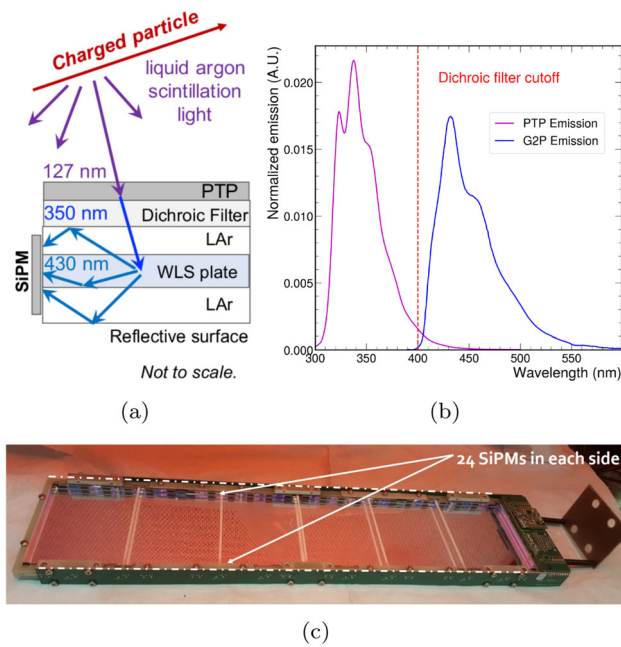


Fig. 2 (a) Schematic of the XA working principle [14]. (b) The dichroic filter cutoff (red dashed line), the pTP (purple line) and the G2P (blue line) emission spectra. (c) Image taken while mounting an FD1 XA of dimensions (50×12)cm²

to the front end electronics by signal leading boards custom designed by INFN Sezione di Milano [15].

Four configurations of these XAs depending on the SiPMs and WLS bar type will be tested in ProtoDUNE. Two different models of SiPMs, from Fondazione Bruno Kessler (FBK) and Hamamatsu Photonics K.K (HPK), will be employed. The particular models are: FBK Triple-Trench (TT) [16], which pixel size is about $50 \mu\text{m}$, and HPK (S13360-6075HS-HRQ) $75 \mu\text{m}$ High Quenching Resistance (HQR) [17] both with a total effective area of about 36 mm^2 and specifically designed for being used at cryogenics temperatures (CT). ProtoDUNE-HD also makes use of two different WLS bars, the EJ-286PS and the bar custom designed by G2P. For all the four configurations OPTO [18] dichroic filters were used. In Table 1 we summarize the four combinations installed in ProtoDUNE-HD that have been characterized in this work.

3 Methodology and instrumentation

Quantifying the absolute efficiency is fundamental for DUNE, as this parameter is needed to fully characterize the PDS. The PDE must be assessed at the operative conditions, at CT and with 127 nm photons. For this reason, we submerged the XA in LAr together with a low-activity electro-deposited ^{241}Am alpha source. Two experimental setups have been established to carry out this measurement, at CIEMAT (Madrid, Spain) and at Milano-Bicocca University (Milan,

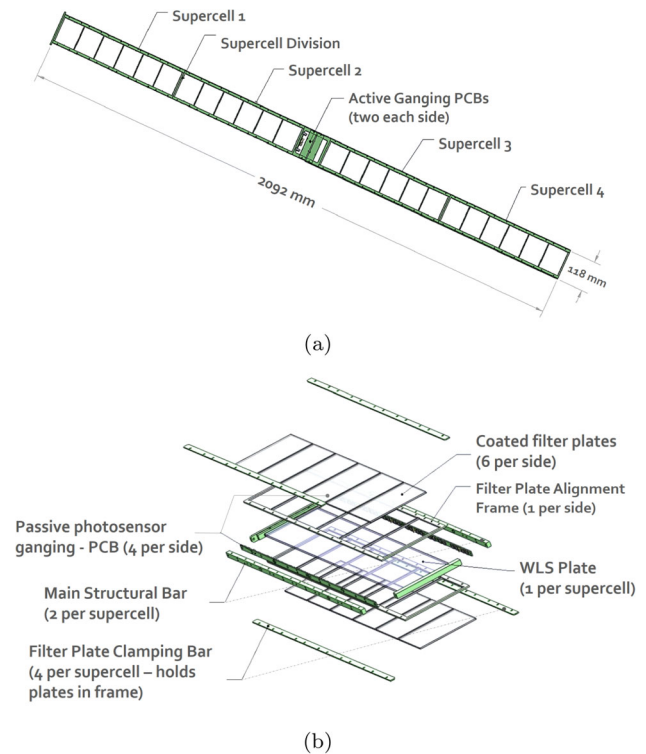


Fig. 3 (a) PDS module including 4 XA cells. (b) Schematic of the assembly process with the different components [14]

Table 1 The four XA configurations installed in ProtoDUNE-HD

	SiPMs	WLS bar	Testing site
(A)	FBK TT	EJ-286PS-1	CIEMAT + MiB
(B)	FBK TT	G2P-FB165A	MiB
(C)	HPK 75HQR	EJ-286PS-1	CIEMAT
(D)	HPK 75HQR	G2P-FB165A	CIEMAT + MiB

Italy). To measure the absolute efficiency of the XA, the number of photons arriving at its surface need to be known. Two different methods have been considered: comparing the amount of light collected by the XA with the light detected by a calibrated photosensor, and estimating the light in the XA from the α -source energy and the known number of scintillation photons per MeV produced in LAr once the solid angle sustained by the source is determined. Both setups liquefy high purity argon gas (GAr) inside a cryogenic vessel.

The data processing and acquisition (DAQ) system configuration, involving the software and the electronics, is similar in both setups and a diagram is shown in Fig. 4

The 48 SiPMs are passively grouped at the input of a trans-impedance amplifier located at the top of the XA, the so-called *cold-amplifier*. The amplifier is based on a SiGe bipolar transistor (Infineon BFP640) followed by a fully differential operational amplifier (Texas Instruments THS4531), and is designed for low noise at low power, giving a voltage

Table 2 Relative distances from the α -source to the sensors and sizes of the box's holes

	XA	Ref. SiPM
Effective area (mm ²)	415.47	36.00
Distance to the source (mm)	29.0 ± 0.7	26.9 ± 0.3

provides light from LEDs and lasers to check the response of the system. In Table 2 we summarize the detectors' dimensions and positions in the box.

The VUV4 SiPMs were calibrated at room temperature by the manufacturer; however, several studies [22–24] have shown a decrease of about 50% in the PDE at CT and a dependence with the incident angle. Considering the results of these studies and the measurements carried out in CIEMAT labs [25] with these sensors exposed to VUV light at different angles, we will assume a PDE of $(11.17 \pm 1.3)\%$ at 127 nm and, 87 K and 4 V overvoltage (OV) for the model S13370-6075CN of VUV4 SiPMs from HPK. The cross-talk probability computed in [25] for the reference SiPMs at CT is $P_{XT} = (14.84 \pm 0.24)\%$ which is in perfect agreement with the result presented in [22].

The XA signal provided by the warm-electronics is digitized by the ADC (model CAEN DT5725S [26]). The signals of the two reference SiPMs are amplified and digitized by the same CAEN module. The trigger is done at ADC level and is provided by the signal in coincidence of the two reference SiPMs. The final output consists of 20 μ s waveforms with 4 ns sampling. A pre-trigger of 2 μ s allows the determination of the baseline on a event-by-event basis. For calibration runs, a pulse generator provides an external trigger and synchronously pulses the light source (laser or LED). Three- μ s waveforms are recorded in the calibration runs with the same time sampling.

3.2 INFN Milano Bicocca setup

The INFN Milano-Bicocca (MiB) setup is an extension of the one used for the PDE measurements of the XA device adopted by the SBND project [27]. The work [13] allowed us to precisely assess the superior performance of the SBND-XA device equipped with the custom produced PMMA based WLS [11], that is now adopted as the baseline component for both the DUNE FD1 and FD2 Photon Detection systems. The setup, the procedures and the method are described in detail in [13].

Figure 6 shows the XA located at the center of the stainless steel ~ 251 cylindrical chamber of 250 mm diameter and 550 mm height. The closed chamber is located in an open 70 l dewar. The chamber is first outgassed down to $O(10^{-4})$ mbar and then connected to a bottle of GAR grade 6.0. The open dewar is filled with LAr and the GAR liquefaction process

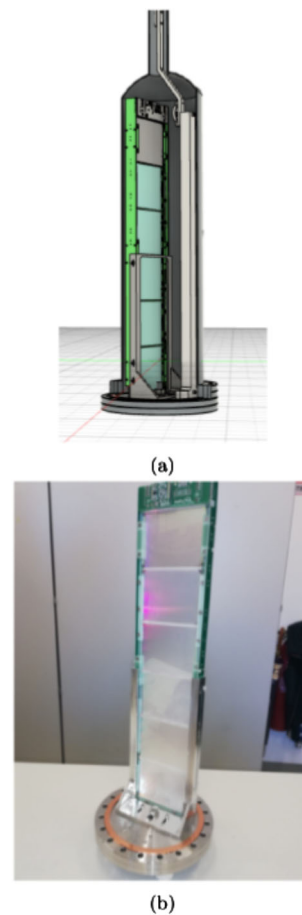


Fig. 6 (a) The scheme of the INFN-MiB setup for the longitudinal scanning and PDE determination of the XA. (b) Picture before closing the chamber

starts inside the chamber. Both the GAR flow and its liquefaction rate in the chamber are sustained by the regulation of the bottle pressure reducer. The exposed ^{241}Am α -source (3.7 kBq) is mounted on the tip of a magnetic manipulator (rototraslator) and allowed to slide on a vertical rail, facing the XA at the distance of (55 ± 1) mm. This allows to scan the PDE of the XA along its z-axis and to monitor with high precision the LAr level inside the chamber during the whole filling process, as the alpha light pulse amplitude greatly increases when the source is in LAr.

The target operational condition is reached when the XA and the front end readout circuit are submerged in LAr. Due to the lack of GAR, in few runs we couldn't reach the top of the device, hence only the data from the scanning positions fully submerged by LAr are considered in the PDE data analysis.

The digitizer (CAEN DT5725 250 MS/sec 14 bits) is self-triggered by setting a threshold, that provides a trigger rate of about 1 kHz for the α -particles and 100 Hz for the muons runs respectively.

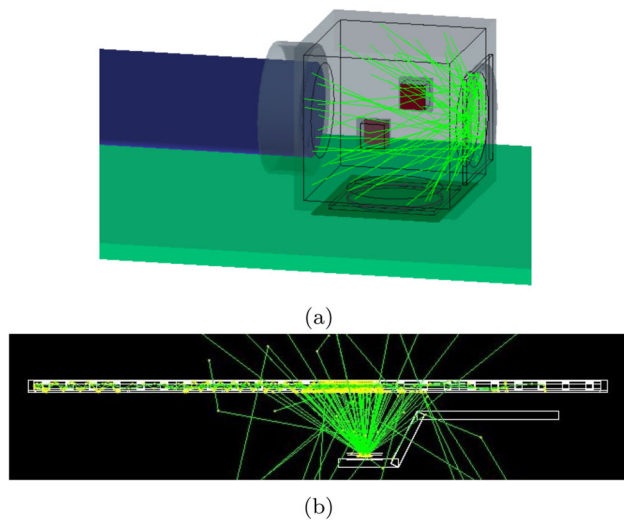


Fig. 7 Example of events generated for (a) CIEMAT and (b) Milano-Bicocca setups

3.3 Monte Carlo simulations

To properly assess the PDE of the XA prototype, a dedicated GEANT4 [28] Monte Carlo (MC) simulation was developed for each setup. For both of them, the scintillation photons generated by the alpha particle energy loss in LAr are emitted uniformly and isotropically, and the MC provides the number of photons reaching the XA acceptance window. For the CIEMAT setup the reference photosensors solid angles are also determined by the simulations and for both MiB and CIEMAT the geometrical acceptances uncertainties are computed by varying both the position and dimensions of the setup elements within their precision errors.

Figure 7a shows the simulation of the CIEMAT setup with the dimensions presented in Table 2. The two reference VUV4 SiPMs (red), the PMT (blue) and the XA (green) are configured as sensitive materials to retrieve the number of detected photons depending on their position with respect to the source. The surrounding black box is designed with a black plastic material that fully absorbs the photons. Each event of the alpha source is simulated to have the number of photons in a random position within the sensitive area. We have determined a systematic error due to the geometrical acceptance uncertainty of 10.8%.

Figure 7b shows a side view of the XA long edge side of the Milano Bicocca MC geometry. About 500 photons are drawn for visualization purposes. The ^{241}Am deposited surface exposed to LAr is embedded in a source holder whose shape and size is included in the MC model to determine the effective light cone. The geometrical acceptance is then driven by the device-to-source distance, that is measured (5.5 ± 0.1) cm, along the whole rail length. The uncertainty on the geometrical acceptance accounts for $\sim 7\%$ and rep-

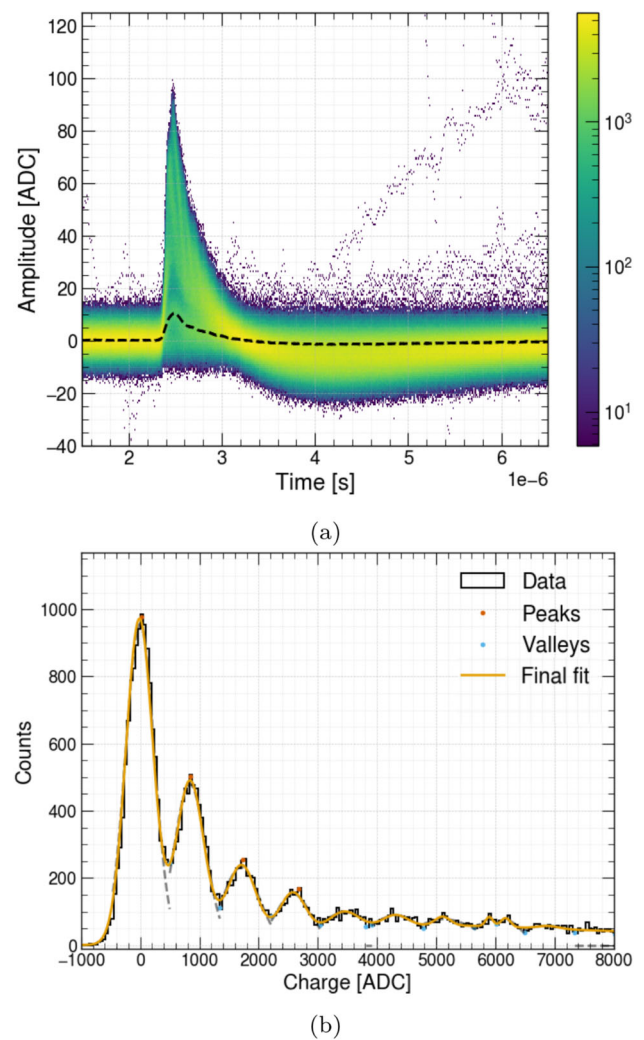


Fig. 8 (a) Persistence histogram of selected waveforms together with the average waveform of one single PE. (b) Charge histogram of selected peaks, the gain is defined by the distance between the first and the second peak

resents the major systematic error for the MiB method. The LAr optical properties are simulated too but for optical path in LAr of $(O(10\text{ cm}))$ both the absorbance and the Rayleigh scattering are negligible.

4 Data analysis

4.1 Calibration

To measure the PDE, the light pulse generated in LAr by ^{241}Am alpha particles and collected by the photosensors must be calibrated by the integrated charge of the single photon electron, i.e. by the gain factor of the SiPMs. The gain depends on the operative temperature and bias voltage, and can be affected by the *fatigue effect*, like for the photo-

Table 3 Experimentally measured SNR of the XA SiPMs at a given overvoltage (OV) and corresponding photon detection efficiency (PDE)

OV	PDE	SNR
(a) FBK TT		
3.5	40	2.40 ± 0.08
4.5	45	3.42 ± 0.07
7.0	50	3.76 ± 0.05
(b) HPK HQR75		
2.0	40	2.90 ± 0.03
2.5	45	3.55 ± 0.02
3.0	50	4.24 ± 0.02

multiplier tubes [29]. In both the CIEMAT and the MiB setup the calibrations are performed with low intensity blue light emitting sources.

Typical calibration waveforms for the XA are displayed in Fig. 8a. The gain is determined from the integrated charge distribution, as shown as an example in Fig. 8b and defined as $\text{Gain} = (\mu_2 - \mu_1)$ where μ_n is the mean value of the Gaussian corresponding to n photoelectrons. The good signal-to-noise ratio (SNR) allows the identification of the peaks corresponding to 1, 2, 3 to N PE and then the gain determination.

The SNR qualifies the capability to detect a single PE (SPE) over the system noise: it depends both on the XA electronics and on the setup related disturbances. We define $\text{SNR} = \frac{\mu_1 - \mu_0}{\sqrt{\sigma_0^2 + \sigma_1^2}}$ from the integrated charge distribution where σ_n is the Gaussian width of the n th peak (0 is the baseline noise peak, 1 is the 1PE peak). For each photosensor type, Table 3 reports the SNR measured for three overvoltage bias values. In all cases a $\text{SNR} > 2$ was measured, hence in all the measurements the SPE detection capability is verified.

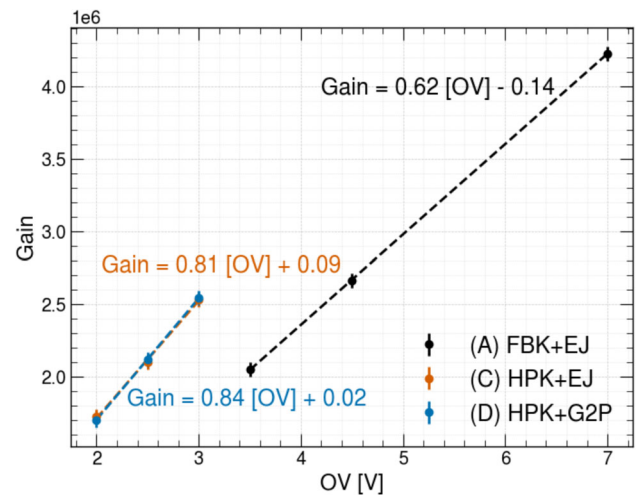
Figure 9 features the measured gain versus over-voltage of XAs equipped with different SiPM models. The gain is a characteristic of the SiPM and independent of the rest of the XA elements.

Dedicated cross-talk studies have been performed by the PDS Consortium for the two SiPMs models deployed in the XAs. The measured cross-talk probabilities (P_{XT} , probability to have a second pixel activation after a true photo electron) are presented in Table 4 for three OV bias values and are used to compute the correction for the efficiency.

The cross-talk correction factors (f_{XT}) used for the analysis are computed as follows:

$$f_{\text{XT}} = \frac{1}{1 + P_{\text{XT}}} \pm \frac{\Delta P_{\text{XT}}}{(1 + P_{\text{XT}})^2}. \quad (1)$$

To assess the XA PDE and compare the performances of the different configurations, we choose the bias OV value of 4.5 OV for FBK TT and 3.0 OV for HPK HQR75, since for

**Fig. 9** Gain versus bias voltage. Dashed lines represent linear fits of the experimental points. Unit conversion to get adimensional gain values was made using the amplifier's gain and the electron charge**Table 4** Experimentally measured cross-talk probabilities at CT

OV	PDE	P_{XT} (%)
(a) FBK TT		
3.5	40	12.68 ± 0.27
4.5	45	16.05 ± 0.32
7.0	50	32.47 ± 0.47
(b) HPK HQR75 from [30]		
2.0	40	6.6 ± 0.7
2.5	45	9.0 ± 1.0
3.0	50	11.0 ± 1.0

these values the two models exhibit similar gain (see Fig. 9) while keeping the $P_{\text{XT}} < 20\%$.

The average waveforms for the SPE are computed for each XA configuration and the results are shown in Fig. 10 for both MIB and CIEMAT setups.

The front-end electronics provides bipolar signals with a characteristic zero crossing time of $1.0 \mu\text{s}$. Due to this behaviour we integrate only the positive part of the signal. The LAr light emission time profile has a triplet component with characteristic emission time $\tau_t \sim 1.6 \mu\text{s} > 1.0 \mu\text{s}$, so to assess the integral of the charge lost in the negative lobe two methods are considered: either the alpha/muon waveforms are deconvolved (CIEMAT) by the SPE response, or the scintillation time profile is convoluted with the SPE response (MiB). The fraction of positive lobe charge is corrected after this computation.

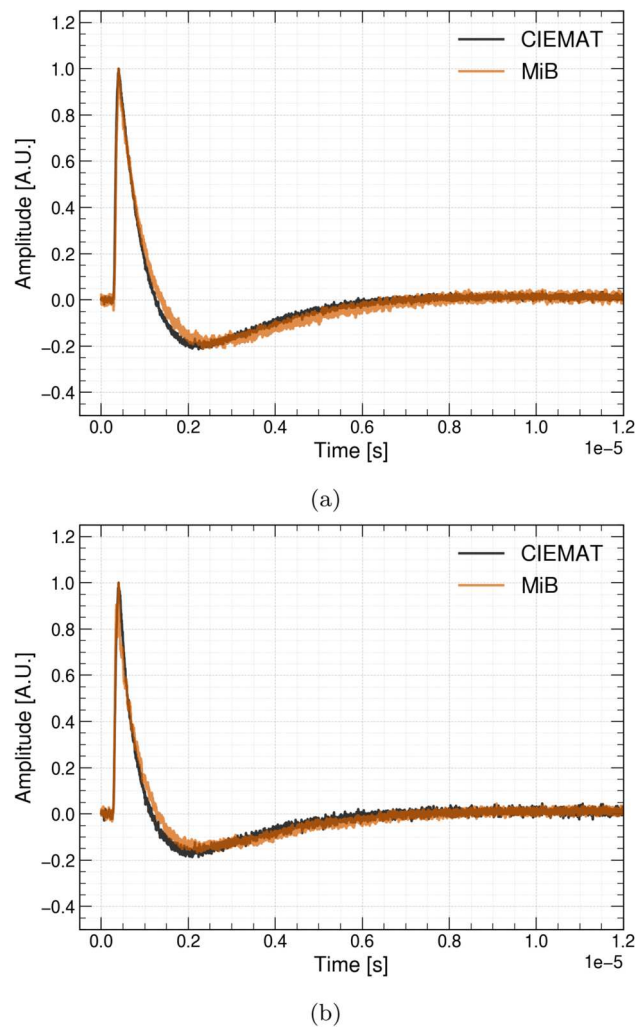


Fig. 10 Single photo-electron normalized response obtained during calibration in CIEMAT and Milano-Bicocca setups. XAs with (a) FBK and (b) HPK SiPMs

4.2 Milano Bicocca analysis

In the method adopted at MiB and used as secondary method by CIEMAT, the XA efficiency ($\epsilon_{\text{MiB}}(\text{XA})$) is computed from the ratio of the detected ($\#PE(\text{XA})$) to the expected ($\#Ph$) light:

$$\epsilon_{\text{MiB}}(\text{XA}) = \frac{\#PE(\text{XA})}{\#Ph} \cdot f_{\text{corr}}. \quad (2)$$

where $\#Ph$ is:

$$\#Ph = LY_{\text{LAr}} E_{\alpha} \Omega = 35700 \text{ ph/MeV} \cdot 5.48 \text{ MeV} \cdot \Omega, \quad (3)$$

The maximal LAr light yield for alpha particles in LAr $LY_{\text{LAr}} = (35700 \pm 2157) \text{ photons/MeV}$ including the α quenching factor $q_{\alpha} = (0.70 \pm 0.04)$ is from [31,32], while the geometrical acceptance (Ω) is determined by the

Monte Carlo simulations discussed in Sect. 3.3. $\#PE(\text{XA})$ is derived from the fit of the full energy peak of the calibrated alpha spectra as described later in this section.

The alpha spectra are the histograms of the alpha waveforms selected by pulse shape discrimination criteria (PSD) [13] and charge integrated over 1000 ns. Figure 11a shows the capability of the MiB setup and method for particle identification by PSD when cutting on the fraction of the prompt (charge integral < 600 ns) over the total (charge integral < 1000 ns), named hereafter f_{prompt} . Muons and alphas are clearly separated in the (f_{prompt}) vs total charge plane: alphas have $f_{\text{prompt}} > 0.7$ and muons $f_{\text{prompt}} < 0.7$. More details on the alpha spectra analysis are provided later on in this section.

The correction factor (f_{corr}) is the product

$$f_{\text{corr}} = f_{\text{XT}} \cdot f_{\text{int}} \cdot f_{\text{purity}}. \quad (4)$$

and takes into account the cross-talk (f_{XT}), the fraction of light falling in the waveform positive lobe (f_{int}) and the effective LAr light yield (f_{purity}), the latter being related [33] to the light quenching impurity (e.g. N_2) concentration that may vary at each filling of the experimental chamber.

The correction for the effective LAr yield (LY_{eff}) is relevant for the absolute PDE determination and to fairly compare the PDE of the different XA configurations. Up to several ppm values the impurities affect only the triplet (or slow) component of the LAr emission that for alpha particles accounts for only 23% of the LY_{LAr} . The re-normalization factor (f_{purity}) accounts for the fraction of the actual triplet (τ_{exp}) to the maximal (τ_{pure}) component [33]

$$f_{\text{purity}}^{-1} = A_{\text{slow}} \frac{\tau_{\text{exp}}}{\tau_{\text{pure}}} + A_{\text{fast}}, \quad (5)$$

where $A_{\text{fast}} = 0.77$ and $A_{\text{slow}} = 0.23$ are the literature singlet and triplet contributions for alphas and $\tau_{\text{pure}} = 1600$ ns is the triplet time constant for the maximal LAr LY [13,32].

At each filling of the experimental chamber i.e. for each of the tested XA configurations, the τ_{exp} is extracted from the muon waveforms analysis. A muon run is taken with the source located at the top position to limit the number of alpha events triggering the DAQ and muons waveforms are selected by PSD criteria: the selected muon waveforms are individually deconvoluted by the SPE waveform template and the resulting normalized muon average waveform is fitted by a two exponential function convoluted with a Gaussian, providing τ_{exp} as shown in Fig. 11b. The τ_{exp} , hence the quality of the LAr, is monitored and found to be stable along the alpha data taking time.

The τ_{exp} measured ranges are reported in Table 5 for each XA configuration together with the the corresponding $f_{\text{int}} \cdot f_{\text{purity}}$.

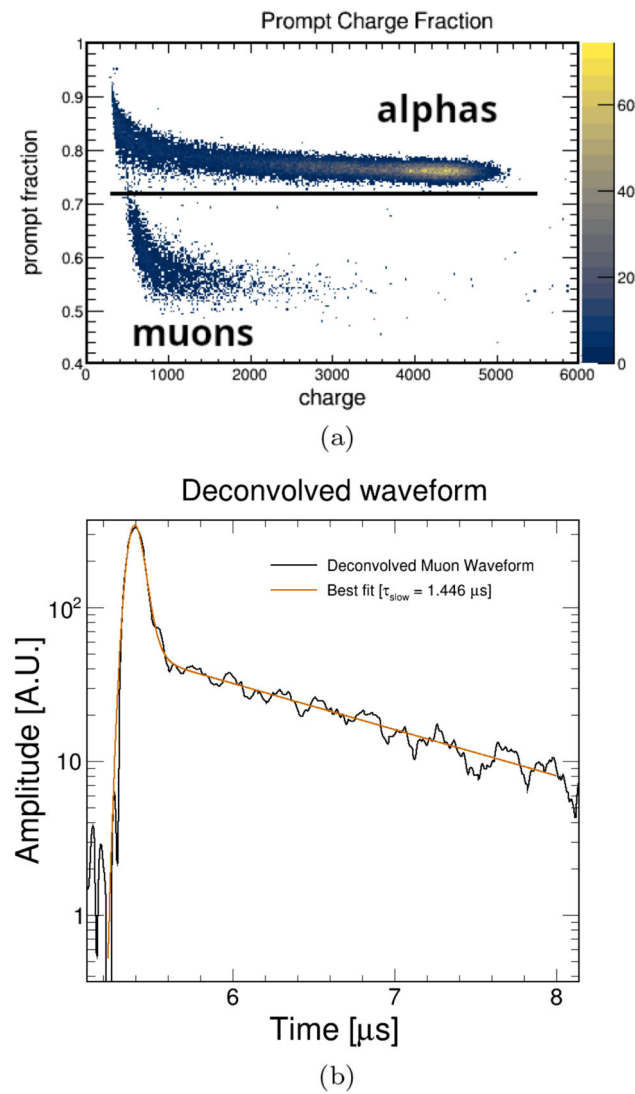


Fig. 11 (a) Fraction of prompt over total integrated charge for an alpha run; alpha and muons populations are clearly distinguishable by cutting on the prompt fraction. (b) The deconvolved muon waveform measured with the MiB setup

Table 5 The LAr triplet decay time constant τ_{exp} ranges derived from the muons analysis and the corresponding combined correction factor for the three measurements with the MiB setup, computed for the best fit in the range

Measurement		τ_{exp} [ns]	$f_{\text{int}} \cdot f_{\text{purity}}$
(A)	FBK + Eljen	910–1113	0.843
(B)	FBK + G2P	910–1115	0.843
(D)	HPK + G2P	1407–1507	0.853

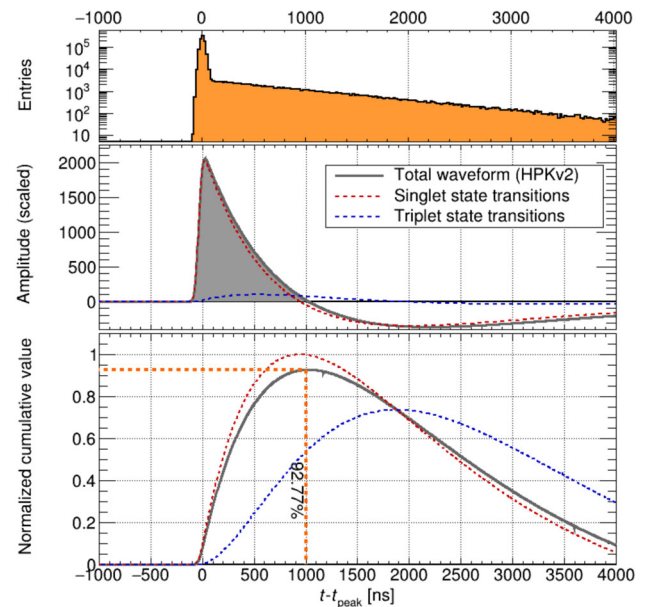


Fig. 12 Computation of the charge integration correction factor for $\tau_{\text{exp}} = 963$ ns. From top to bottom: simulated time profile, time profile convolved with electronics response, fraction of integrated charge (y axis) as a function of the integration time (x axis). $f_{\text{int}} = 92.77\%$ is found for a 1000 ns integration window

The waveform bipolar shape requires to assess the actual charge integrated within the positive lobe of the alpha waveforms (f_{int}), that is in turn anti-correlated to f_{purity} and τ_{exp} ; in fact at the increase of the latter and since it is greater than the waveform zero crossing time, a larger fraction of the late photons are lost since they fall into the waveform negative lobe. Therefore the $f_{\text{int}} \cdot f_{\text{purity}}$ is numerically computed as follows and described in Fig. 12: the alpha particle scintillation time profile for a given τ_{exp} , (top panel), is convoluted with the SPE template and provides the expected pulse shown in the middle panel. The integration correction factor (f_{int}) is finally reported in the Fig. 12 (bottom) as a function of the integration time: at each time, it is the ratio of the grey area of the middle panel (the cumulative of the positive lobe of the convoluted waveform) to the orange area of the top panel (the integral of the entire raw scintillation signal). As an example, a $\tau_{\text{exp}} = 963$ ns gives $f_{\text{int}} = 92.77\%$ for a 1000 ns integration time and $f_{\text{purity}} = 90.84\%$. The $f_{\text{int}} \cdot f_{\text{purity}}$ factor is then applied to the alpha pulse height spectra to properly assess the absolute PDE. The error on $f_{\text{int}} \cdot f_{\text{purity}}$ is computed by varying τ_{pure} and τ_{exp} and found to be $< 2\%$; as reported in Table 5 their product is stable for τ_{exp} ranging from 900 to 1500 ns.

Figure 13a shows the module geometrical acceptance as a function of the source position; the values are retrieved by the Montecarlo GEANT4 simulations described in Sect. 3.3. Two calibrated (by SPE charge) alpha spectra are also shown in Fig. 13b; the difference of the detected photoelectron peak

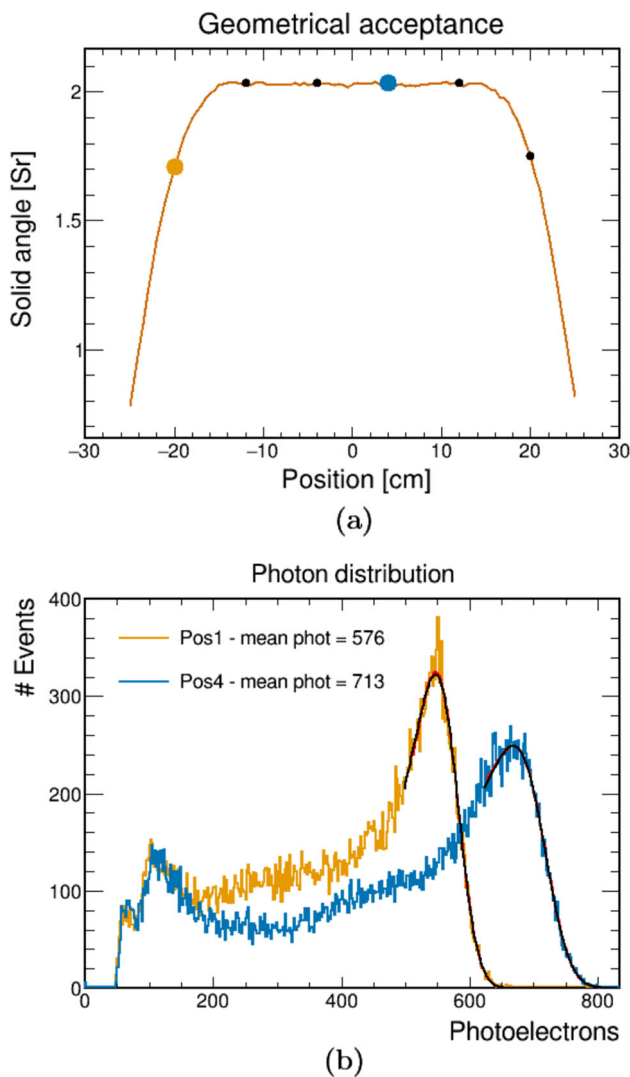


Fig. 13 (a) Geometrical acceptance vs source position relative to the XA center. The orange and blue dots correspond to the positions of the source for the 2 spectra shown in panel b. (b) The alpha spectra measured at the two source positions highlighted in panel a

values is due to the yet uncorrected geometrical acceptances, that are marked with the same color in the plot above. The tail extending to the low energies comes from degraded light events. The alpha full energy peak is fitted with a gaussian convoluted with an exponential, and the number of detected photons is retrieved by the gaussian mean value.

In the MiB setup, the ^{241}Am source can slide along a rail mounted in front of the module under test, allowing to measure the PDE at several positions as shown in the Fig. 14a, to study the module uniformity. Figure 14b, c and d report the measured PDE against the source position for each of the three studied XA configurations. For the positions below 20 cm the PDE looks systematically, despite not significantly, lower than at higher positions. This behaviour is more pronounced for the FBK measurements. All the mea-

Table 6 Results for the absolute efficiency ($\epsilon_{\text{MiB}}(\%)$)

(A)	(B)	(C)	(D)
1.80 ± 0.15	2.22 ± 0.19	–	2.40 ± 0.20

surements have been performed with the same module frame and dichroic filters, the only variables being the SiPMs boards (FBK or HPK) and the light guide (G2P or Eljen). For both HPK and FBK, the observed decrease in efficiency at the lowest positions could be explained by a non optimal SiPM-light guide coupling due to the tolerances of both the frame and light guides. The more evident decrease for FBK could be explained by a lower photon detection efficiency of one (few) SiPMs facing that region; this can happen if they have a higher breakdown voltage, hence a lower gain at the same bias voltage. The results obtained with the MiB setup are summarized in Table 6.

The repeated measurements of the HPK & G2P show a high reproducibility: in Fig. 14d, three independent measurements performed in different days and with two different LAr fillings report that the efficiencies measured at the same positions are well within one standard deviation. This suggests that the main error source are the systematics, as the geometrical acceptance and the cross talk probability uncertainties, while the run to run variance is low. The errors reported in Table 6 are to be considered for the absolute PDE, while the relative differences among the tested configurations have lower errors.

4.3 CIEMAT analysis

In the method used by CIEMAT, the efficiency of the XA, $\epsilon_{\text{MAD}}(\text{XA})$, is obtained from the known efficiency of the reference SiPM's, $\epsilon(\text{Ref.SiPM})$, as is shown in Eq. 6.

$$\epsilon_{\text{MAD}}(\text{XA}) = \frac{\#PE_{\text{u.a.}}(\text{XA})}{\#PE_{\text{u.a.}}(\text{Ref.SiPM})} \cdot \epsilon(\text{Ref.SiPM}) \cdot \frac{\Omega_{\text{u.a.}}(\text{XA})}{\Omega_{\text{u.a.}}(\text{Ref.SiPM})} \cdot f'_{\text{corr}} \quad (6)$$

where, u.a is used for the variables computed per unit area, $\#PE_{\text{u.a.}}$ is the number of PE and f'_{corr} is a correction factor that includes the cross-talk correction (f_{XT}) and the fraction of light not included in the waveform integration (f'_{int}). The different responses to the extension of the source depending on the sensitive area of the detector are included in $[\Omega_{\text{u.a.}}(\text{XA})/\Omega_{\text{u.a.}}(\text{Ref.SiPM})]$. This geometrical acceptance (Ω) is obtained with the Monte Carlo introduced in Sect. 3.3.

The acquisition in the CIEMAT setup is triggered when the amplitude of both reference SiPMs is above a certain threshold. In Fig. 15 the amplitudes of the two SiPMs are shown for a threshold of 1 PE (22 ADC); the light from the α -source is clearly distinguishable and allows to set the

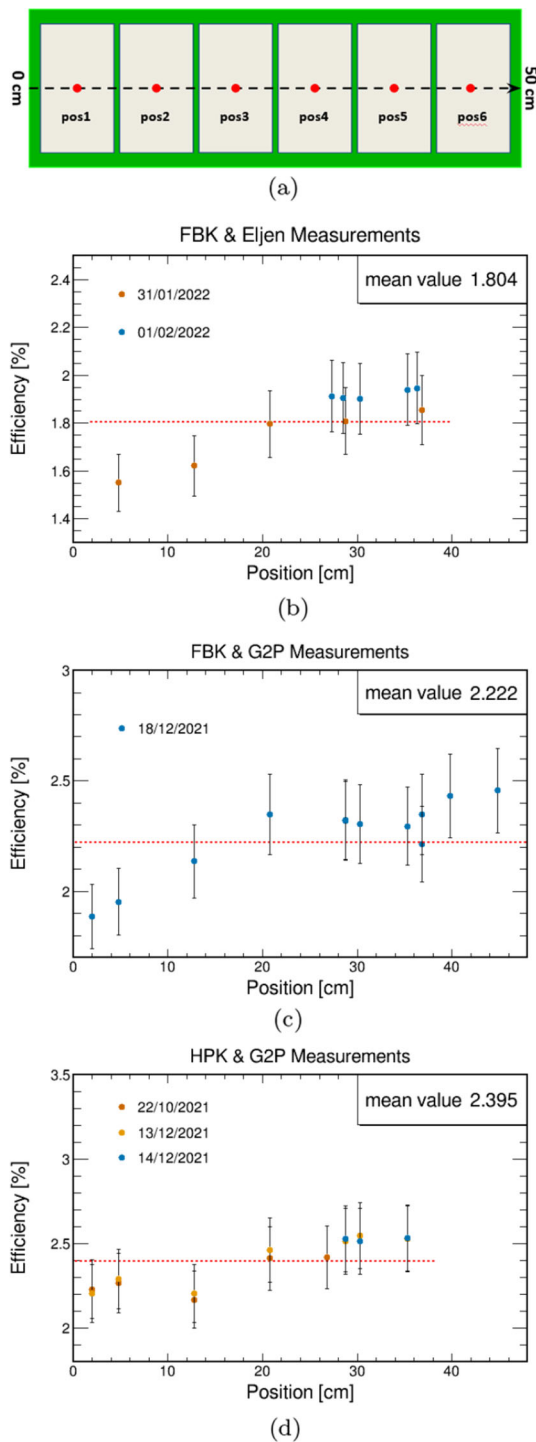


Fig. 14 (a) Scheme of the XA irradiation positions. (b, c, d) The measured PDE for vs the source positions, for different device configurations (HPK-FBK and G2P-Eljen)

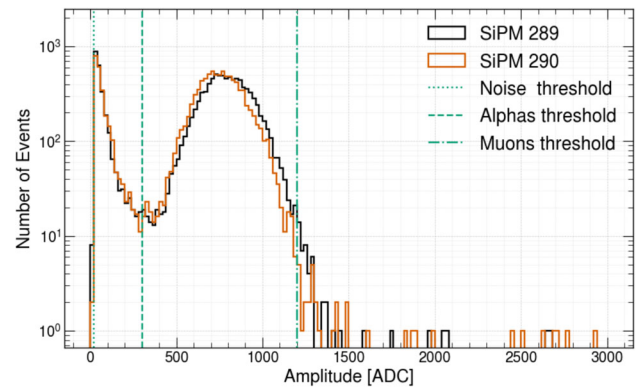


Fig. 15 Amplitude histogram for both reference VUV4 SiPM where we can see the different thresholds used for acquiring noise (22 ADC), alpha (300 ADC) and muons (12000 ADC) events

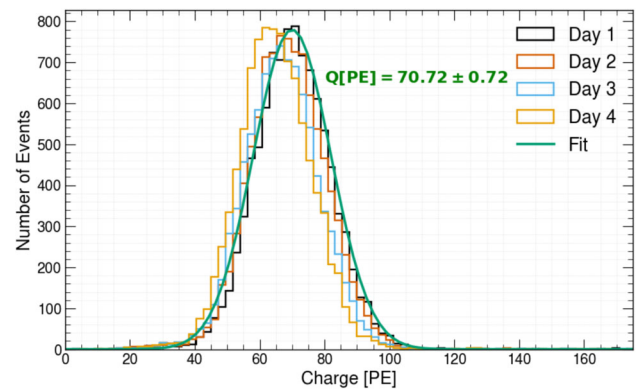


Fig. 16 FBK+EJ XA α -spectrum for OV 4.5 V and the different days of data taking. Additionally, a gaussian fit for the first day is shown

threshold for triggering α events as marked in the plot (300 ADC). The trigger rate is about 26 Hz in agreement with half of the source activity (considering 2π α emission). Due to the small size of the box and the alpha source rate, the number of muon events is small enough not to interfere with the alpha signal although they are filtered by amplitude.

The α -spectrum detected by the XA upon the SiPMs triggering is displayed in Fig. 16. These distributions are fitted to Gaussian functions, estimating the number of detected PEs as the mean of the distribution.

In this case, the XA plus electronics response is deconvolved of the light signal profile to determine the full charge and compute f'_{int} . The pure XA response is obtained from a 405 nm laser signal; a Gaussian filter is applied in the Fourier space to remove high frequency components. An example of a deconvolved waveform is shown in Fig. 17.

By comparing the integrated charge before and after the deconvolution is performed we obtain:

$$f'_{\text{int}} = 1.09 \pm 0.02. \quad (7)$$

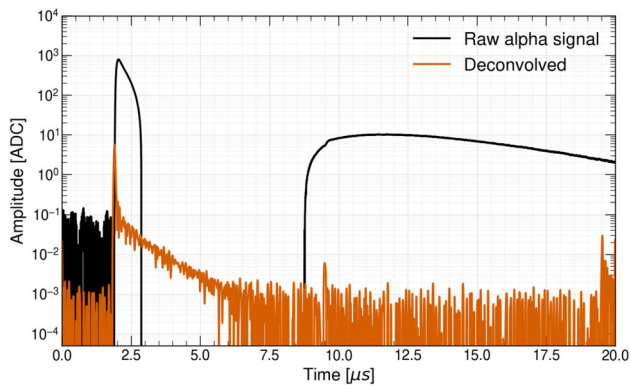


Fig. 17 XA raw and deconvolved average waveform of alpha signal for the HPK+G2P configuration. The deconvolution process remove the undershoot that is part of the XA response leaving the expected LAr scintillation profile

Table 7 Results for the geometrical acceptance of the XA and the VUV4 reference SiPMs in [Sr] and per unit area (u.a.)

	XA	Reference SiPM
Ω (Sr)	0.29 ± 0.02	0.034 ± 0.003
Effective area (mm ²)	415.47	36.00
$\Omega_{u.a.}$	6.9 ± 0.5	9.4 ± 0.8

This factor depends on the purity of the setup and on the transfer function of the cold-electronics readout. For CIEMAT setup, the achieved purity for the different measurements remains stable enough to assume an unique correction factor for all the configurations. The deviations are included in the error quoted in Eq. 7. The final correction factor also includes the effect of the cross-talk probability as defined in Eq. 1:

$$f'_{\text{corr}} \equiv \frac{f_{\text{XT}}(\text{XA})}{f_{\text{XT}}(\text{Ref.SiPM})} f'_{\text{int}}. \quad (8)$$

CIEMAT setup allows to compute the absolute efficiency of the XA by a direct comparison between the detected number of PE per mm² of the XA and the HPK VUV4 reference SiPMs. As presented in Eq. 6, the exposure dimensions are different depending on the photosensor and so are the corresponding solid angles. The results are summarized in Table 7.

The ratio of the geometrical acceptances per unit area is:

$$\frac{\Omega_{u.a.}(\text{Ref.SiPM})}{\Omega_{u.a.}(\text{XA})} = 1.35 \pm 0.15. \quad (9)$$

Following Eq. 6 we have obtained values for the efficiency of the XA for each day and campaign with respect to each SiPMs.

Table 8 Results for the absolute efficiency ($\epsilon_{\text{MAD}}(\%)$) with CIEMAT method

(A)	(B)	(C)	(D)
1.34 ± 0.24	—	1.59 ± 0.29	2.13 ± 0.38

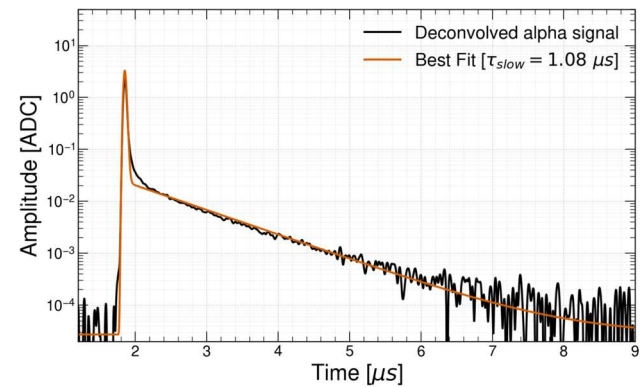


Fig. 18 Alpha VUV4 SiPM scintillation profile fitted with a two-exponential function used to extract the τ_{slow} parameter

Table 9 Results for the absolute efficiency ($\epsilon'_{\text{MAD}}(\%)$) with the MiB method

(A)	(B)	(C)	(D)
1.61 ± 0.12	—	1.86 ± 0.15	2.50 ± 0.21

The final values presented in Table 8 are computed with a weighted average of the values of each day and for each reference SiPM.

The main source of systematics is the reference VUV4 SiPM PDE (14%), followed by the geometrical acceptance (10.8%).

The efficiency has also been computed from the α -source light-yield that it is used as a cross-check (see Eq. 2). As explained in Sect. 4.2, an additional correction accounting for the quenching of the impurities is needed. CIEMAT uses the scintillation profile provided by the reference SiPMs for α -triggered events, as it is shown in Fig. 18. The purity in our setups is good enough to assume linear dependence between the charge and the value of τ_{slow} . In the CIEMAT setup the variation of the purity beyond the linear range can be determined through its effect on the collected charge by the reference SiPMs.

The obtained results following this approach are summarized in Table 9.

5 Results

In this section we summarize the absolute efficiency results for the XA with the two different methods applied see (Table

Table 10 Results for the XA absolute efficiency ($\epsilon_i(\%)$)

	FBK + EJ	FBK + G2P	HPK + EJ	HPK + G2P
ϵ_{MIB}	1.80 ± 0.15	2.22 ± 0.19	–	2.40 ± 0.20
ϵ_{MAD}	1.34 ± 0.24	–	1.59 ± 0.29	2.13 ± 0.38
ϵ'_{MAD}	1.61 ± 0.12	–	1.86 ± 0.15	2.50 ± 0.21

10). In the first (ϵ_{MIB}), the number of detected photons are compared to the Monte Carlo estimates for the described geometry, a PDE scanning along the cell is performed and the average value is provided; for the second one, (ϵ_{MAD}) CIEMAT group made a direct comparison with the reference VUV4 SiPMs known efficiency and measure the PDE at one spot. Additionally, CIEMAT used MiB method as crosscheck (ϵ'_{MAD}) For this purpose, we take the results from Sects. 4.2 and 4.3 (Tables 6, 8 and 9) where we have calibrated and computed the number of detected photo-electrons respectively.

6 Conclusions

In this article, we report the measurement of the absolute detection efficiency of the XA in the dedicated cryogenic setups of MiB and CIEMAT. The two setups attain high purity and reproducible results. Two methods with completely different systematic uncertainties ensure the reliability of the measurement. The XA is the basic unit of the PDS of the first module of the DUNE FD (FD1) and its basic performance and collection efficiency needs to be addressed before its installation in ProtoDUNE, where its global performance will be studied for the first time. Four different XA configurations exist, in terms of SiPM model and WLS bar manufacturer; two of these element combinations were measured in the two labs, providing compatible results within 1σ . The PDE has been measured to be about 2% for a SiPM bias voltage corresponding to a gain of about $2.5 \cdot 10^6$ electrons for both models, i.e., an OV of 3 V for HPK and 4.5 V for FBK SiPMs. The lower value of the PDE is found for the combination FBK and EJ (1.34–1.80)%. The PDE is 10% higher for HPK SiPMs and the same WLS bar. This is under investigation and maybe related to the smaller active area of the FBK sensor (32.8 mm² versus the 36 mm² of HPK). The PDE increases between 24% and 35% with the G2P WLS bar. These measurements show a clear better performance of the XA equipped with G2P bar and call for an optimization of the SiPM and WLS bar optical coupling. Forty units of each of the four tested configurations are installed in ProtoDUNE-HD in the NP04 facility at the CERN neutrino platform, and they will be operated in 2024.

Funding The present research has been supported and funded by INFN in the framework of the DUNE project, the European Union

NextGenerationEU/PRTR, European Union's Horizon 2020 Research and Innovation programme under Grant Agreement No. 101004761, by MCIN/AEI/10.13039/501100011033 under Grants No. PID2019-104676GB-C31, RYC2021-031667-I, PRE2019-090468 and PRE2020-094863 of Spain. Work produced with the support of a 2023 Leonardo Grant for Researchers in Physics, BBVA Foundation.

Data Availability Statement Data will be made available on reasonable request. [Authors' comment: Data acquired and/or analysed during the different campaigns of both institutes is available on reasonable request.]

Code Availability Statement Code/software will be made available on reasonable request. [Authors' comment: The developed code for this study is available on reasonable request.]

Open Access This article is licensed under a Creative Commons Attribution 4.0 International License, which permits use, sharing, adaptation, distribution and reproduction in any medium or format, as long as you give appropriate credit to the original author(s) and the source, provide a link to the Creative Commons licence, and indicate if changes were made. The images or other third party material in this article are included in the article's Creative Commons licence, unless indicated otherwise in a credit line to the material. If material is not included in the article's Creative Commons licence and your intended use is not permitted by statutory regulation or exceeds the permitted use, you will need to obtain permission directly from the copyright holder. To view a copy of this licence, visit <http://creativecommons.org/licenses/by/4.0/>.

Funded by SCOAP³.

References

1. C. Palomares, JINST **18**(02), C02064 (2023). <https://doi.org/10.1088/1748-0221/18/02/C02064>
2. DUNE Collaboration, Deep Underground Neutrino Experiment (DUNE), Far Detector Technical Design Report, Volume I: Introduction to DUNE (2020)
3. DUNE Collaboration, Deep Underground Neutrino Experiment (DUNE), Far Detector Technical Design Report, Volume II: DUNE Physics (2020)
4. DUNE Collaboration, Supernova neutrino burst detection with the Deep Underground Neutrino Experiment (2021). <https://doi.org/10.1140/epjc/s10052-021-09166-w>
5. T. Doke, A. Hitachi, J. Kikuchi, K. Masuda, H. Okada, E. Shimamura, Absolute scintillation yields in liquid argon and xenon for various particles (2002). <https://doi.org/10.1143/JJAP.41.1538>
6. T. Heindl, T. Dandl, M. Hofmann, R. KrÄfÅ'cken, L. Oberauer, W. Potzel, J. Wieser, A. Ulrich, The scintillation of liquid argon (2010). <https://doi.org/10.1209/0295-5075/91/62002>
7. DUNE Collaboration, Deep Underground Neutrino Experiment (DUNE), Far Detector Technical Design Report, Volume III: DUNE Far Detector Technical Coordination (2020)
8. B. Abi et al., JINST **15**(12), P12004 (2020). <https://doi.org/10.1088/1748-0221/15/12/P12004>
9. L. Paulucci et al., JINST **15**, C01047 (2020). <https://doi.org/10.1088/1748-0221/15/01/C01047>
10. Eljen Technology, Wavelength Shifter bar. <https://eljentechnology.com/products/wavelength-shifting-plastics>
11. Glasstopower, Wavelength Shifter bar. <https://www.glasstopower.com/>
12. National Institute for Nuclear Physics (INFN), p. 8 (2023)

13. C. Brizzolari, S. Brovelli, F. Bruni, P. Carniti, C.M. Cattadori, A. Falcone, C. Gotti, A.A. Machado, F. Meinardi, G. Pessina, E. Segreto, H.V. Souza, M. Spanu, F. Terranova, M. Torti, Enhancement of the X-Arapuca photon detection device for the DUNE experiment (2021). <https://doi.org/10.1088/1748-0221/16/09/p09027>
14. DUNE Collaboration, Deep Underground Neutrino Experiment (DUNE), Far Detector Technical Design Report, Volume IV: Far Detector Single-phase Technology (2020)
15. N. Gallice, A. Zani, P. Sala, M. Lazzaroni, M. Citterio, A. Andreani, in *2021 IEEE International Instrumentation and Measurement Technology Conference (I2MTC)*, pp. 1–6 (2021). <https://doi.org/10.1109/I2MTC50364.2021.9459995>
16. Fondazione Bruno Kessler (FBK), FBK SiPM technology. <https://www.fbk.eu/en/>
17. Hamamatsu Photonics K.K. (HPK), Multi-Pixel Photon Counters (MPPCs/SiPMs). <https://www.hamamatsu.com/eu/en/product/optical-sensors/mppc/index.html>
18. Opto electronica s.a, <https://www.opto.com.br/>
19. C. Brizzolari, P. Carniti, C. Cattadori, E. Cristaldo, A. de la Torre Rojo, M. Delgado, A. Falcone, K. Francis, N. Gallice, C. Gotti, M. Guarise, E. Montagna, A. Montanari, G. Pessina, M. Pozzato, J. Smolik, F. Terranova, L. Tomassetti, A. Verdugo de Osa, D. Warner, J. Zalesak, A. Zani, J. Zuklin, V. Zutshi, Cryogenic front-end amplifier design for large SiPM arrays in the DUNE FD1-HD photon detection system (2022). <https://doi.org/10.1088/1748-0221/17/11/p11017>
20. Hamamatsu Photonics K.K. (HPK), PMT (R6836). <https://www.hamamatsu.com/eu/en/product/type/R6836/index.html>
21. E. Calvo Alamillo, M.T. Crespo Vázquez, P.F. Rato Mendes, R. Álvarez Garrote, J.I. Crespo Anadón, C. Cuesta, A. De la Torre Rojo, I. Gil-Botella, I. Martán Martán, M. Mejuto Mendieta, C. Palomares, L. Pérez Molina, J.A. Soto Otón, A. Verdugo de Osa. Validation of electrodeposited ²⁴¹Am alpha-particle sources for use in liquified gas detectors at cryogenic temperatures (2023). <https://doi.org/10.1016/j.apradiso.2023.110913>
22. T. Pershing, J. Xu, E. Bernard, J. Kingston, E. Mizrachi, J. Brodsky, A. Razeto, P. Kachru, A. Bernstein, E. Pantic, I. Jovanovic. Performance of Hamamatsu VUV4 SiPMs for detecting liquid argon scintillation (2022). <https://doi.org/10.1088/1748-0221/17/04/p04017>
23. P. Nakarmi, I. Ostrovskiy, A.K. Soma et al., Reflectivity and PDE of VUV4 Hamamatsu SiPMs in liquid xenon (2020). <https://doi.org/10.1088/1748-0221/15/01/p01019>
24. P. Lv, G.F. Cao, L.J. Wen, S. Al Kharusi, G. Anton, I.J. Arnuist et al., Reflectance of Silicon Photomultipliers at Vacuum Ultraviolet Wavelengths (2020). <https://doi.org/10.1109/tns.2020.3035172>
25. R. Álvarez Garrote, E. Calvo, A. Canto, J. Crespo-Anadón, C. Cuesta, A. de la Torre Rojo, I. Gil-Botella, S.M. Corchado, I. Martán, C. Palomares, L. Pérez-Molina, A.V. de Osa, Nucl. Instrum. Methods Phys. Res. Sect. A Accel. Spectrom. Detect. Assoc. Equip. (2024). <https://doi.org/10.1016/j.nima.2024.169347>
26. CAEN, CAEN Tools for Discovery (2023). <https://www.caen.it>
27. M. Bass, The Short Baseline Neutrino Oscillation Program at Fermilab (2017). <https://doi.org/10.48550/ARXIV.1702.00990>
28. S. Agostinelli et al., GEANT4—a simulation toolkit (2003). <https://geant4.web.cern.ch/>. [https://doi.org/10.1016/S0168-9002\(03\)01368-8](https://doi.org/10.1016/S0168-9002(03)01368-8)
29. W.A. Rosen, F.R. Chromey, Astron. J. **90**, 139 (1985). <https://doi.org/10.1086/113721>
30. M. Andreotti, S. Bertolucci, A. Branca, C. Brizzolari, G. Brunetti, R. Calabrese, P. Carniti, D. Casazza, C. Cattadori, E. Calvo, A. Cervera, S. Chiozzi, V. Cicero, A. Cotta Ramusino, E. Cristaldo Morales, C. Cuesta, R. D'Amico, A. De la Torre, M. Delgado Gonzalez, F. Di Capua, D. Di Ferdinando, A. Dyshkant, M. Eads, A. Falcone, E. Fialova, P. Filip, G. Fiorillo, M. Fiorini, K. Francis, F. Galizzi, N. Gallice, D. Garcia-Gamez, M.Á. García-Peris, T. Giammaria, I. Gil-Botella, C. Giugliano, C. Gotti, M. Guarise, D. Guffanti, M. Kovalcuk, I. Lax, M. Lazzaroni, M. Lokajicek, E. Luppi, S. Manthey, J. Martin-Albo, N. Mauri, L. Meazza, A. Minotti, N. Moggi, E. Montagna, A. Montanari, I. Neri, F.J. Nicolas-Arnaldos, C. Palomares, L. Pasqualini, L. Patrizii, L. Párez-Molina, G. Pessina, V. Pia, F. Poppi, M. Pozzato, M. Querol, J. Rocabado, A. Saadana, P. Sala, A. Sanchez-Castillo, P. Sanchez-Lucas, F.S. Schifano, G. Sirri, J. Smolik, M. Spanu, F. Terranova, M. Tenti, L. Tomassetti, M. Torti, N. Tosi, A. Verdugo de Osa, H. Vieira de Souza, J. Zalesak, B. Zamorano, A. Zani, S. Zucchelli, J. Zuklin, V. Zutshi, J. Instrum. **19**(01), T01007 (2024) <https://doi.org/10.1088/1748-0221/19/01/T01007>
31. T. Doke, Fundamental Properties of Liquid Argon, Krypton and Xenon as Radiation Detector Media (1981)
32. A. Hitachi, T. Takahashi, N. Funayama, K. Masuda, J. Kikuchi, T. Doke, Effect of ionization density on the time dependence of luminescence from liquid argon and xenon (1983). <https://doi.org/10.1103/PhysRevB.27.5279>
33. R. Acciarri, M. Antonello, B. Baibussinov, M. Baldo-Ceolin, P. Benetti, F. Calaprice, E. Calligarich, M. Cambiaghi, N. Canci, F. Carbonara, F. Cavanna, S. Centro, A. Cocco, F. Di Pompeo, G. Fiorillo, C. Galbiati, V. Gallo, L. Grandi, G. Meng, C. Vignoli, Effects of Nitrogen and Oxygen contamination in liquid Argon (2009). <https://doi.org/10.1016/j.nuclphysbbs.2009.10.037>